Synthesis of Trimetallic (Ni-Cu)@Ag Core@Shell Nanoparticles without Stabilizing Materials for Antibacterial Applications

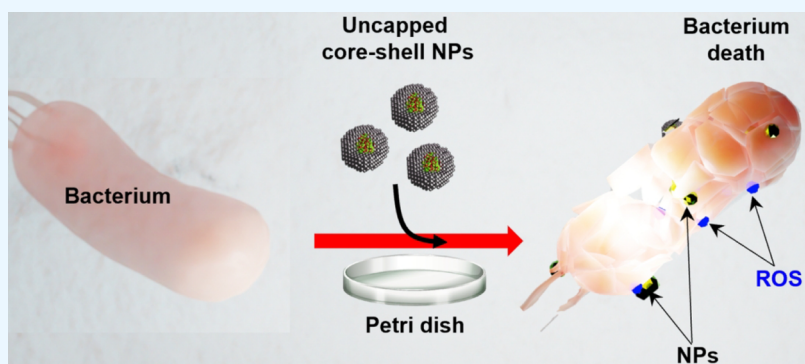Abdullah A. A. Ahmed,* Thana S. Aldeen, Samar A. Al-Aqil, ZabnAllah M. Alaizeri, and Saad Megahed

ACCESS | Metrics & More | Article Recommendations | Supporting Information

ABSTRACT: We report a simple method to prepare colloidal trimetallic (Ni-Cu)@Ag core@shell nanoparticles (NPs) without stabilizing materials. Experimental evidence was found for the successful synthesis of these NPs using X-ray diffraction (XRD), optical spectroscopy, and high-resolution transmission electron microscopy (HRTEM). The presence of core metals (Ni and Cu) was confirmed by elemental analysis using a total reflection X-ray fluorescence (TXRF) analysis. In addition, the absorption spectra of the prepared samples exhibited broad bands compared to the bands of the monometallic NPs, indicating the formation of a core−shell nanostructure. The antibacterial activity of the trimetallic NPs was evaluated against three Gram-negative (*Pseudomonas aeruginosa*, *Escherichia coli*, and *Salmonella*) and two Gram-positive (*Streptococcus* and *Staphylococcus aureus*) bacteria on Mueller−Hinton agar. These NPs showed high inhibition of bacterial growth at the low sample concentrations used in this study compared to other nanomaterials. One of the interesting results of the current study is that the inhibition zone of *Pseudomonas aeruginosa* as a resistant bacterium was high for most NPs. These results make the prepared samples promising candidates for antibiotic material applications.

1. INTRODUCTION

With the beginning of the 21st century, medical challenges began to increase. Among these challenges is the antibiotic resistance of many bacteria.[1] This is a very worrying trend that has contributed to the re-emergence and development of dangerous infections, especially in nosocomial settings, and thus represents one of the greatest threats to human health.[2] Finding efficient alternatives to these antibiotics has become urgently necessary as a result. Metallic nanomaterials have attracted the interest of scientists and could be one of the alternatives, as their toxicity mechanism is oxidative stress,[3,4] which could be caused by the generation of reactive oxygen species (ROS) on the designed nanomaterials.[4]

Some of the most promising nanoparticles are the silver nanoparticles (Ag NPs) due to the many applications of Ag NPs such as electronics, chemical catalysis, biosensing, and surface-enhanced Raman spectroscopy; Ag NPs are also used as effective antimicrobial agents.[5−7] For medical equipment and various consumer products such as plastics, textiles, cosmetics, food containers, and personal care products, Ag NPs have been incorporated as antibacterial agents.[8,9] Nickel (Ni NPs) have also been used as antibacterial agents due to their ability to generate singlet oxygen, which enhances the antibacterial activity.[10] Copper (Cu NPs) exhibit significant inhibitory activity against Gram-positive and -negative bacteria.[11] The combination of two or more metals enhances the antibacterial activity against different types of bacteria.[12]
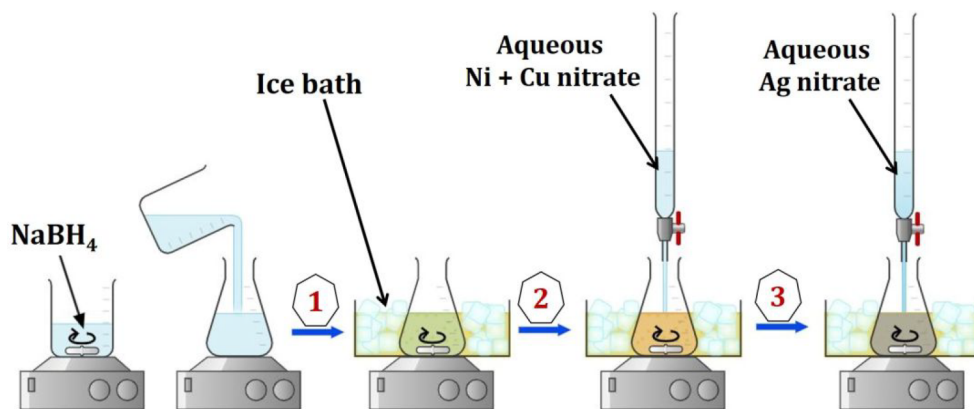
Although metal NPs, including silver NPs, have many biological applications, Ag NPs can easily penetrate the skin when the functional barrier is disrupted and cause cellular damage and cytotoxicity. The toxicity of Ag NPs seems to be closely related to their concentration but may vary in different

Figure 1. Experimental procedures to synthesize (Ni-Cu)@Ag core@shell colloidal NPs.

species.[13,14] Ag NPs have two properties (aggregation and ionization) once they come into contact with biomolecules in solution. While increased ionization leads to increased potential toxicity, increased aggregation has the effect of decreasing toxicity. This could be due to the fact that aggregation reduces the dissolution surface area, resulting in fewer Ag ions on the surface of the nanoparticles.[15,16] Therefore, we can assume that there is an additional significant effect related to the ionization and aggregation phenomena of Ag NPs in bimetallic and trimetallic forms.

Core@shell NPs have attracted the interest of many researchers because they are versatile and can be modified for different applications by changing the nature or composition of the core and shell material. Furthermore, core@shell NPs have additional advantages in comparison to the simple NPs such as biocompatibility, lower cytotoxicity, and easy of discarding.[17] The combination of Ni and Ag NPs showed higher inhibition for the growth of *K. pneumoniae* strains than thae mixture of other NPs.[12] The antibacterial rate against *E. coli* was improved by Ni@Ag NPs to 88% compared to a commercial agent because the Ag shell with the presence of Ni in the core allows easy magnetic separation of the core−shell from the reaction mixture.[18] Yang and co-workers showed that Au@Ag NPs enhanced antibacterial activity against *S. aureus* compared with Au NPs due to the release of Ag+ ions from the shell, which increased the generation of ROS. Moreover, Au@Ag NPs showed negligible toxicity to human dermal fibroblasts with concomitant enhancement of antibacterial activity against *S. aureus*.[19] The Ag/Cu molar ratio of Cu@Ag NPs showed better antibacterial activity on *S. aureus* than on *E. coli*, as the Gram-negative bacterium is more susceptible due to its thin membrane.[20] Recently, Sarkar and co-workers presented how Cu@Ag NPs on aluminosilicate geomaterials enhance antibacterial activity.[21]

The conventional method to synthesize metallic core@shell NPs is a two-step/multistep route: namely, a reduction of the core precursors and a subsequent formation of the shell layer.[22,23] Another common approach for a significant portion of core−shell particles is polymerization of shells on preformed cores.[24,25] In addition, a one-step method for fabricating core@shell NPs has been developed. The core and shell precursors are capable of forming the core@shell NP under the same reaction conditions.[26,27] There have also been various other approaches such as self-assembly, electrojetting, one-step Stöber, direct deposition, and ultrasonic spray pyrolysis methods.[28]
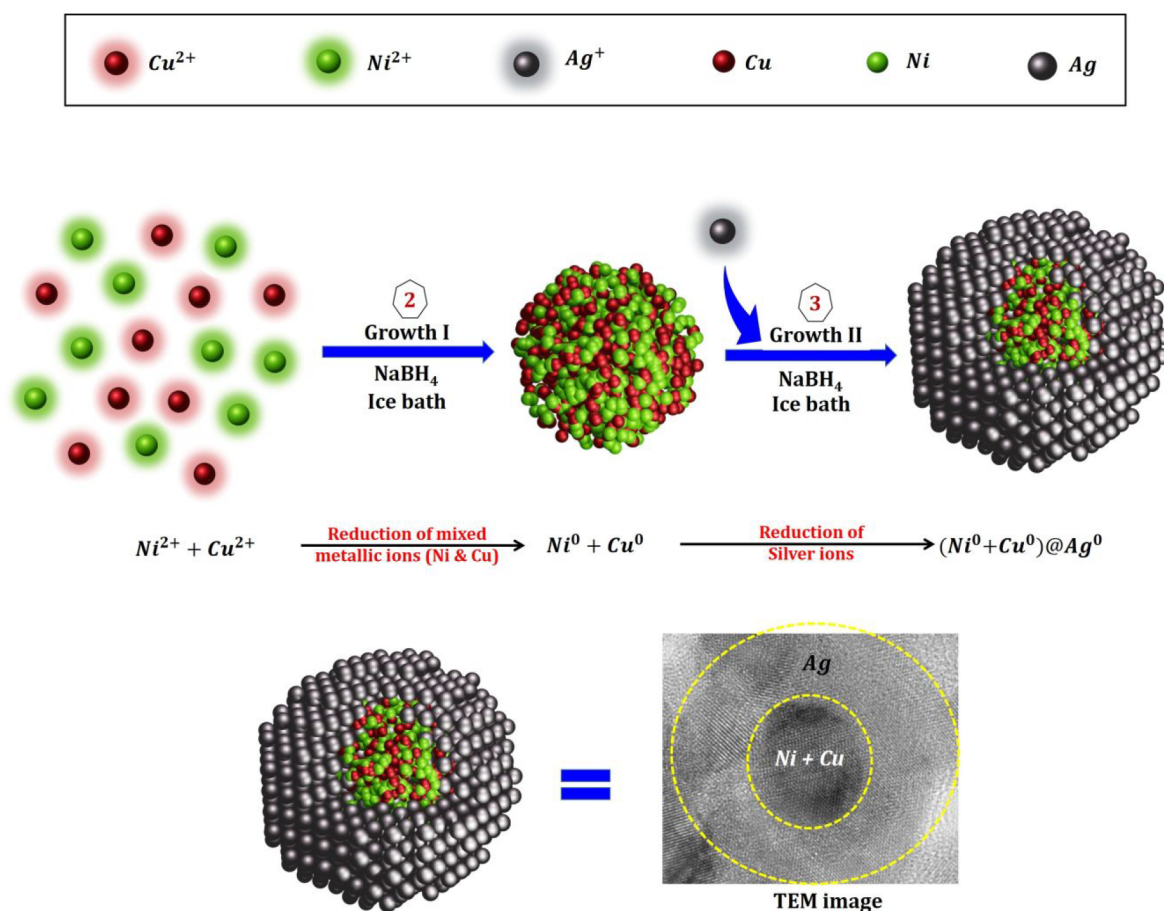
In the current study, we fabricated colloidal trimetallic (Ni-Cu)@Ag core@shell NPs without capping agents. These NPs were designed such that the core was composed of a mixture of Ni and Cu metals with different contents, while the shell was composed of Ag in all samples. The antibacterial activity against different bacterial species was investigated.

2. EXPERIMENTAL SECTION

2.1. Chemicals. Silver nitrate (Sigma-Aldrich, 99.5%), copper nitrate trihydrate (BDH Chemicals, Extra purification), nickel nitrate hexahydrate (Fluka, 98%), cadmium nitrate tetrahydrate (Hayashi Pure Chemical, 97%), and sodium borohydride (Fluka, 97%) were used without additional purification. Deionized water was used as the solvent for all of the prepared solutions.

2.2. Synthesis of (Ni-Cu)@Ag Core@Shell Colloidal NPs. A sodium borohydride, $NaBH_4$ (2 mM, 272.4 mg in 3600 mL of deionized water), solution was prepared, and then it was poured into an Erlenmeyer flask which was placed in an ice bath and stirred constantly for about 30 min. Separately, 1 mM solutions for each of the three metallic precursors were prepared (204 mg for Ag nitrate, 348.9 mg for Ni nitrate, and 289.2 mg for Cu nitrate) into 1200 mL of deionized water. The volume of the added metallic precursors was varied between the core metals (Ni and Cu), while the metal shell (Ag) was fixed at 50% of the total volume (1200 mL) for all samples. For the (Ni-Cu)1@Ag sample, 15% (180 mL) of Ni nitrate solution and 35% (420 mL) of Cu nitrate solution were mixed and added dropwise into a stirred $NaBH_4$ aqueous solution at rate of about 1 drop/s. After that, 50% (600 mL) Ag nitrate was added drop by drop into the previous mixed solutions, as shown in Figure 1. For the (Ni-Cu)2@Ag NPs, the volume of Ni and Cu nitrate solutions was 25%. For the (Ni-Cu)3@Ag NPs, the volumes of Ni and Cu nitrate solutions were 35% and 15%, respectively. The Ag nitrate solution was 50% for all samples. During the addition of the Ag nitrate solution, the mixed solution turned dark brown, dark yellow, and yellow, respectively. When the addition of Ag nitrate solution was finished, the stirring was stopped and the magnetic bar was removed. In this step, the final colloidal NP solution was obtained, which was confirmed by UV−visible spectra of the prepared colloidal NPs. It was then stored for further use in a dark place to avoid exposure to light.

We now present a simple method for synthesizing a mixture of two metals (Ni and Cu) in the core and a silver shell without using a polymer, capping agent, or other organic chemicals. By stepwise addition of Ni and Cu salts in the presence of a reducing

$Ni^{2+} + Cu^{2+}$ —Reduction of mixed metallic ions (Ni & Cu)→ $Ni^0 + Cu^0$ —Reduction of Silver ions→ $(Ni^0 + Cu^0)@Ag^0$

Figure 2. Schematic representation of the mechanism of formation of colloidal (Ni-Cu)@Ag NPs with a TEM image of a sample (bottom). The numbers 2 and 3 with the reaction steps refer to the numbers in Figure 1.

agent (NaBH$_4$) and an ice bath, the Ni^{2+} and Cu^{2+} ions were reduced to form the core of the NPs (steps 1 and 2 in Figure 1). By slowly adding a silver nitrate solution to the mixture (step 3 in Figure 1), the Ag$^+$ ions were reduced to Ag and adsorbed on the outer surface of the core metals, forming a thick shell. This mechanism is shown schematically in Figures 1 and 2.

2.3. Characterizations. The structural properties of prepared core@shell NPs were examined using X-ray diffraction (XRD) techniques (XD-2 X-ray diffractometer using Cu Kα radiation (λ = 1.54) at 36 kV and 20 mA, China). For XRD measurements, the prepared colloidal NPs were dried to get samples in a powder form and then XRD was carried out. The concentrations of each element in the samples were measured using a total reflection X-ray fluorescence (TXRF) spectrometer (Bruker S2 PICOFOX) at room temperature. Field emission transmission electron microscopy (FETEM) (JEOL JEM-2100F) with an operating voltage of 200 kV was used to measure the particular size of the prepared NPs. Normal- and high-resolution (HR) TEM images were also acquired to observe the crystallinity of the NPs as found in the HR-TEM texture of typical crystals. The suspension of ultrasonically treated trimetallic NPs was placed on a carbon-coated copper grid, air-dried, and observed by FETEM. The elemental composition of the NPs was determined by energy dispersive X-ray spectrometry (EDS). The size distribution of NPs was calculated from HRTEM images using ImageJ software. Absorbance spectra of samples were obtained using a UV−vis

spectrophotometer (SPECORD 200) at room temperature in the wavelength range of 190−1100 nm.

2.4. Antibacterial Activity. The antibacterial activity of trimetallic (Ni-Cu)@Ag core@shell NPs was investigated against three Gram-negative (*Pseudomonas aeruginosa*, *Escherichia coli*, and *Salmonella*) and two Gram-positive (*Streptococcus* and *Staphylococcus aureus*) bacteria on Mueller−Hinton agar. The zone of inhibition (ZOI) was evaluated using a Vernier caliper. Details of the preparation of the Muller−Hinton agar plates, the test sample, and the mechanism of antibacterial activity are explained in the Supporting Information.

The required amount (38 g) of Muller−Hinton agar (Himedia) was accurately weighed and dissolved in 1000 mL of distilled water in a 2000 mL Erlenmeyer flask. It was stirred gently with a glass rod to dissolve the contents uniformly. The Erlenmeyer flask was then sealed with a tight cotton stopper after ensuring that the pH of the medium was adjusted to the pH required for effective bacterial growth (7.3 ± 1). The Muller−Hinton agar thus dissolved was sterilized in an autoclave at 121 °C and 15 lbs of pressure for 15 min. The sterilized medium was cooled to 45 °C. Then, about 15 mL of the medium was poured into sterile Petri dishes under aseptic conditions (under laminar air flow) until the depth of the medium was approximately 4 mm. Then the poured Mueller−Hinton agar plates were left to solidify. The solidified plates were further used for antibacterial testing after quality control for contamination. Wells with a diameter of 4 mm and a depth of 4 mm were made in the Muller−Hinton agar plates, into which the bacterial inoculums
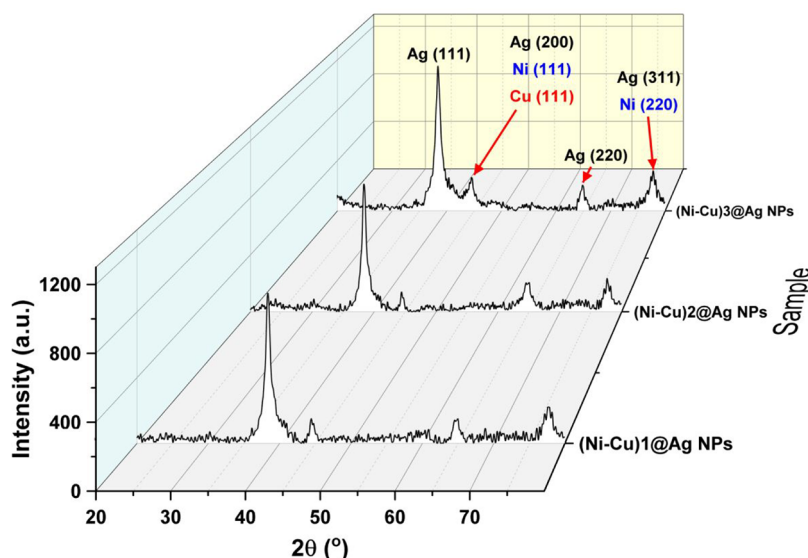
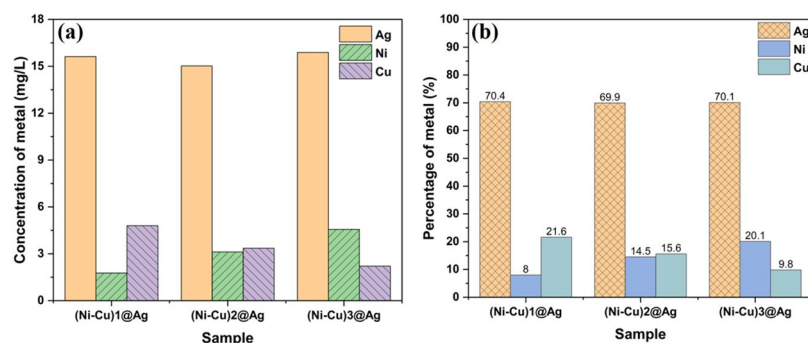**Figure 3.** XRD patterns of (Ni-Cu)@Ag core@shell NPs.

Figure 4. TXRF results of (Ni-Cu)@Ag core@shell NPs: (a) concentration of metals in mg/L; (b) percentage of each metal per sample.

were spotted and to which the sample was then added at different concentrations in the respective wells. The antibacterial sensitive inhibition zones were measured.

3. RESULTS AND DISCUSSION

3.1. XRD Analysis. Figure 3 shows the XRD patterns of the trimetallic (Ni-Cu)@Ag core@shell NPs. Four strong diffraction peaks were distinguished by the lattice reflections of (111), (200), (220), and (311) of the face-centered-cubic (fcc) Ag-3C, space group $Fm\bar{3}m$. These patterns matched those of JCPDS Card No. 04-0783.[29] The broad pattern centered at around $2\theta = 44.498°$ for all NPs was due to the presence of lattice reflections at (111) and corresponded to Ni and Cu. These patterns were in agreement with JCPDS Card Nos. 04-0850 (Ni),[30] and 85-1326 (Cu).[31] On the other hand, the weakness of the peaks of the core metals (Ni or Cu) was attributed to the formation of a thick metal shell (silver). These results confirmed that trimetallic core@shell NPs were successfully formed. These results agree with those in the literature.[32−34] Also, Figure 3 shows XRD patterns with low intensity and broad diffraction peaks due to the nanonature of the prepared samples. In comparison with the core metal phases (Ni and Cu), it is clear that the Ag phase is a dominant phase due to the thick shell of NPs that formed. Moreover, the diffractions (111) of Cu and Ni are located close to (200) of Ag, which resulted in a broad peak for the three samples, as shown in Figure S1. These results confirmed that the trimetallic core@shell NPs were successfully formed.

The average crystallite sizes of the prepared (Ni-Cu)1@Ag, (Ni-Cu)2@Ag, and (Ni-Cu)3@Ag NPs, calculated using the Scherrer equation, were found (9, 8.4, and 6.9 nm, respectively). The variation in crystallite size could be explained in terms of the ionic radii of metals, which were 83 pm for Ni^{2+} and 87 pm for Cu^{2+} (or 91 pm for Cu^+).[35] As the Cu content in (Ni-Cu)1@Ag, (Ni-Cu)2@Ag, and (Ni-Cu)3@Ag decreased from 35% to 15%, respectively, the crystallite size decreased from around 9 to 6.9 nm. This indicated that an decrease in the ionic radius of the core metal resulted in a decrease of the crystallite size. This variation was ascribed to the change in metal content within the entire NPs. This result could be confirmed by a comparison with the average crystallite sizes of bimetallic core@shell NPs, which were 7 nm for Ni@Ag NPs and ∼21 nm for Cu@Ag NPs (Figure S1, inset). The close values of the ionic radii of core metals (Ni and Cu) resulted in close values for the crystallite sizes of three samples. Also, the calculated crystallite sizes of the NPs prepared by the Williamson−Hall (W−H) method was 7.5, 6.1, and 3.4 nm for (Ni-Cu)1@Ag, (Ni-Cu)2@Ag, and (Ni-Cu)3@Ag, respectively (Figure S2), confirming the variation in crystallite size as a function of the ionic radii of the metals noted above. Specific surface areas (SSAs) were calculated for the prepared samples using XRD analysis. They were found to be 32.9, 35.4, and 43.1 m^2/g for (Ni-Cu)1@Ag, (Ni-Cu)2@Ag and (Ni-Cu)3@Ag, respectively, as given in Table S1. Compared with the bimetallic NPs, the SSA values of the trimetallic NPs were between the SSA values of Cu@Ag and Ni@Ag, which was
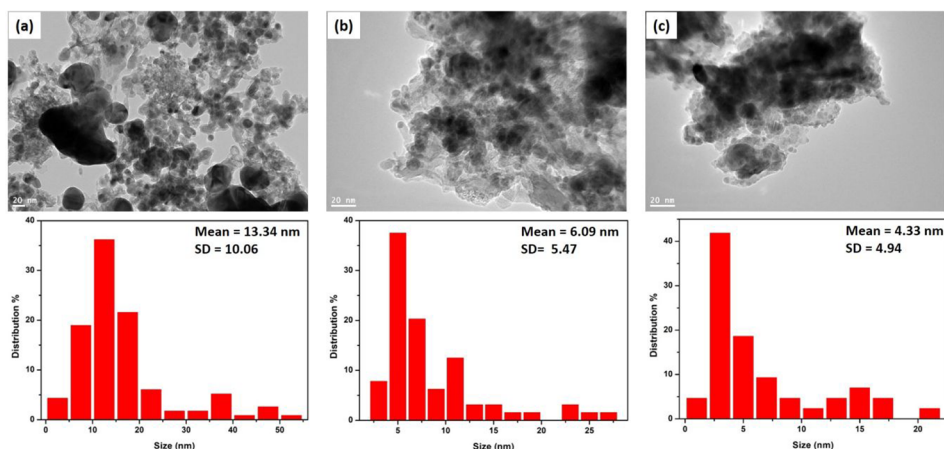
Figure 5. TEM images with their corresponding histograms for (a) (Ni-Cu)1@Ag, (b) (Ni-Cu)2@Ag, and (c) (Ni-Cu)3@Ag NPs.

related to the crystallite size of the NPs (Figure S3). The calculated SSA using this method is in good agreement with values of Ag NPs obtained by BET techniques.[36]

3.2. Elemental Analysis. The results of the elemental chemical analysis of prepared samples performed by TXRF for Ni, Cu, and Ag are presented in TXRF spectra (Figure S4) and histograms (Figure 4). There is a significant estimation of Ni and Cu by TXRF for all the samples. TXRF spectra exhibited Ni and Cu elements at 7.48 and 8.05 keV, respectively, which lie under the Ni K12 and Cu K12 lines, respectively. Ag metal lies under Ag L1 (at 2.98 keV). The quantitative description of TXRF can be seen in Figure 4a. The metal concentration indicates the existence of each metal per sample. For (Ni-Cu)1@Ag, the percentages of Ni and Cu metals was 8% and 21.6%, while they were 20.1% and 9.8%, respectively, for the (Ni-Cu)3@Ag sample, as shown in Figure 4b. (Ni-Cu)1@Ag has almost the same percentage (around 15%). These results showed that the percentage for each metal measured via TXRF is in good agreement with the proposed starting quantities of the metallic precursors.

An energy dispersive X-ray spectroscopy (EDS) analysis of the prepared NPs was performed, as shown in Figure S5. The elemental Ag was present in high quantities at ∼3.1 keV, Ni at ∼7.5 keV, and Cu at ∼8.1 keV. The metallic percentaged of the samples were 20.6%, 37.9%, and 41.5% for Ni, Cu, and Ag, respectively, for (Ni-Cu)1@Ag NPs, 25.4%, 31%, and 43.5% for Ni, Cu, and Ag, respectively, for (Ni-Cu)2@Ag NPs, and 37.2%, 20.7%, and 42.2% for Ni, Cu, and Ag, respectively, for (Ni-Cu)1@Ag NPs. From the results of EDS, it can be seen that the samples were prepared in good compatibility with the theoretical percentages of metals in the core and shell of the three trimetallic NPs.

3.3. TEM Analysis. Figure 5 gives TEM images of the prepared samples with distribution histograms of the nanoparticles. TEM images illustrated that the particles have spherical and semispherical shapes. The average particular size decreased from 13.34 to 4.33 nm as the Cu content decreased from 35% to 15% for the prepared samples. The decrease in the particle size could be explained by the fact that the ionic radius of the core metal leads to a decrease in the particle size, which was accompanied a the decrease in Cu content as explained previously in section 3.1. Moreover, it is noted that there is agreement between the XRD and TEM results with regard to the variation and size of prepared samples.

Figure 6 gives HRTEM images of the trimetallic core@shell NPs that were taken at higher magnification. The mix of core metals (Ni and Cu) looked like dark spherical particles, while the shell was a light low-intensity region surrounding the core. These results could be confirmed by SAED analysis for the patterns for core and shell metals. HRTEM images with a SAED analysis of the core@shell provided evidence of a core−shell structure of all the samples consisting of Ni and Cu as cores and Ag as a shell.

3.4. Absorbance Spectra. Plasmon bands are unique physical properties of nanoparticles. The surface plasmon resonance (SPR) is mainly determined by the dielectric properties of the metal and the surrounding medium, as well as the particle size and shape.[37] The location of plasmon absorption bands of metallic NPs depended on the size and shape of nanostructures. The characteristic peaks for SPR of Ag, Cu, and Ni NPs were obtained at 400, 571, and 210 nm, respectively (Figure S6), which indicate the formation of monometallic NPs.[38−40]

The absorption spectra of (Ni-Cu)@Ag colloidal NPs presented SPR bands in the range 400−420 nm, which corresponds to the Ag shell (Figure 7). The broader SPR bands compared with those of monometallic Ag NPs can be explained by the extended Mie theory for core@shell metallic NPs and can be attributed to the Ag nanometric layer which covers both Ni and Cu cores.[41] Also, it was observed that an absorbance shoulder appeared at around 540 nm, especially for (Ni-Cu)1@Ag and (Ni-Cu)2@Ag samples, due to SPR of the higher content of Cu in the core. These results confirmed the presence of Cu in the dispersed samples. The presented results are in good agreement with core@shell metallic reports.[38,42]

Pinto and co-workers studied the stability of Ag-NPs prepared in aqueous medium by measuring UV−vis spectra for Ag-NPs after a long storage (1 year). They found that the intensity of the UV−vis spectra of the samples increased with increasing storage time.[43] This is due to the surface oxidation of Ag-NPs, so that the intensity of the plasmon absorption peaks increased as the degree of oxidation of Ag-NP decreased. This result was also supported by Yin et al., who showed a red shift of λ_{max} of the plasmon absorption peaks due to the change in shape of the silver nanoparticles.[44] Our results are in agreement with these results showing that the intensity of the UV−vis spectrum increased after 3 months of storage, as shown in Figure S7. It was clear that the SPR became broader due to the change in shape
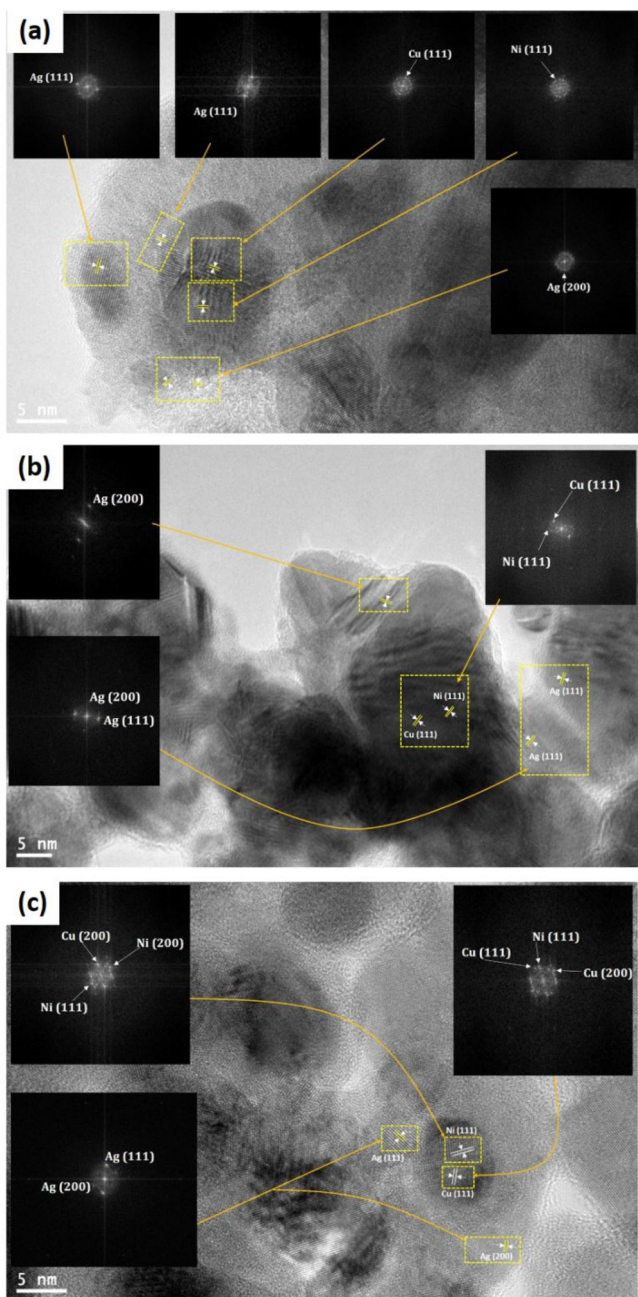
Figure 6. HRTEM images with SAED analysis for (a) (Ni-Cu)1@Ag, (b) (Ni-Cu)2@Ag, and (c) (Ni-Cu)3@Ag NPs.

and size of the prepared samples, which could be due to aggregation.

3.5. Antibacterial Activity. The antibacterial activity of the prepared samples was investigated against three Gram-negative (*Pseudomonas*, *Escherichia coli*, and *Salmonella*) and two Gram-positive (*Staphylococcus aureus* and *Streptococcus*) bacterial pathogens on Mueller–Hinton agar (Figure 8). The antibacterial abilities of the synthesized bimetallic and trimetallic core@shell NPs were examined through an agar-based well diffusion technique. The zone of inhibition (ZOI) was evaluated using Vernier calipers. To demonstrate the trimetallic NP effect against these bacteria, we also presented bimetallic (Ni@Ag and Cu@Ag) NP effects as comparison tests.

The growth inhibition of the core@shell NPs against five bacteria is shown in Figure 9. For *E. coli*, it is clear that (Ni-
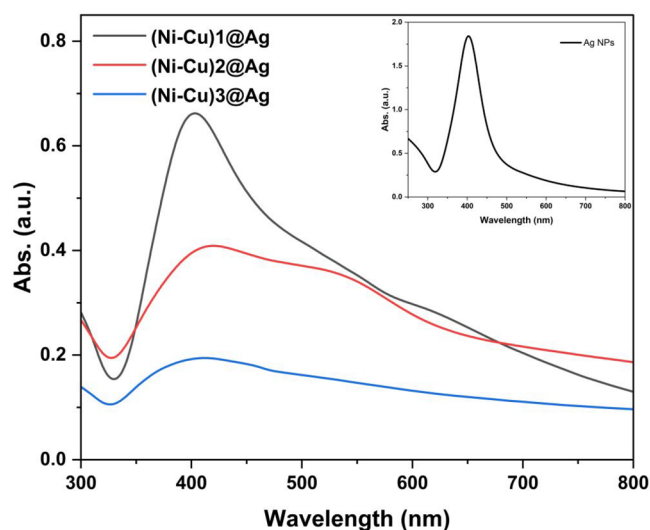

Figure 7. Absorbance spectra of prepared samples. The inset is the absorbance spectrum of pure Ag colloidal NPs.

Cu)1@Ag NPs had the highest antibacterial activity levels for all concentrations with a ZOI of 34 mm. This activity is higher than those in many previous studies that have been reported for *E. coli*.[45−47] On other hand, Ni@Ag presented the lowest levels with a ZOI of around 5 mm. Generally, trimetallic NPs exhibited improved antibacterial activity over bimetallic samples, especially (Ni-Cu)1@Ag and (Ni-Cu)2@ NPs. The bi- and trimetallic NPs had high levels (26−36 mm) of antibacterial activity against a resistant bacteria (*Pseudomonas aeruginosa*), as shown in Figure 9b. Trimetallic NPs had enhanced antibacterial activity levels (36 nm). The activity against *Salmonella* showed that Ni@Ag had the highest levels of antibacterial activity (ZOI reached up to 28 mm at 60 μg/mL). The antibacterial activity of Ni@Ag and (Ni-Cu)3@Ag against *Staphylococcus aureus* was the highest, and that of (Ni-Cu)1@Ag against *Streptococcus* was highest as shown in Figure 9d,e.

Figures 9 and 10 exhibited comprehensive images regarding the antibacterial activity enhancement of the prepared samples against five types of bacteria. On the one hand, the samples showed that they had activity with all examined bacteria, as there was a high effect of at least one trimetallic sample with each type of bacteria, as shown in Figure 10 (red dashed circles). On the other hand, the samples showed that they are not specific to one or two types of the examined bacteria, and this gives them the advantage that they are comprehensive samples over all the examined bacteria. For example, (Ni-Cu)1@Ag NPs are effective for *E. coli*, *Salmonella*, and *Streptococcus*, (Ni-Cu)2@ Ag NPs are effective for *E. coli*, *Pseudomonas aeruginosa*, and *Streptococcus*, and (Ni-Cu)3@Ag NPs are effective for *Pseudomonas aeruginosa* and *Staphylococcus aureus*.

Core−shell NPs have antibacterial activity because they either interact directly with bacteria cells or form secondary products that destroy the bacterial cell wall. Antibacterial activity is caused by two factors: (a) the production of reactive oxygen species (ROS) and (b) the release of heavy-metal ions. On the surface of metal nanoparticles, photogeneration of ROS such as hydrogen peroxide (H_2O_2), hydroxyl radicals ($^{\bullet}OH$), singlet oxygen ($^1O_2$), and superoxide radical anions ($O_2^{\bullet-}$) has occurred due to the surface plasmon resonance.[10]

ROS are mostly produced in organelles such the mitochondria and the endoplasmic reticulum.[48] Naturally, ROS are generated
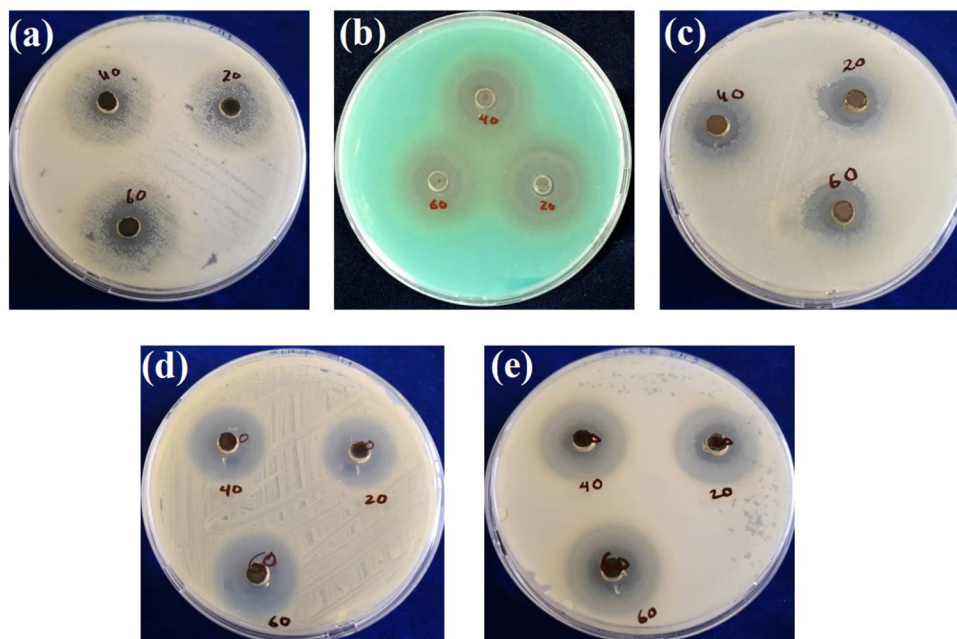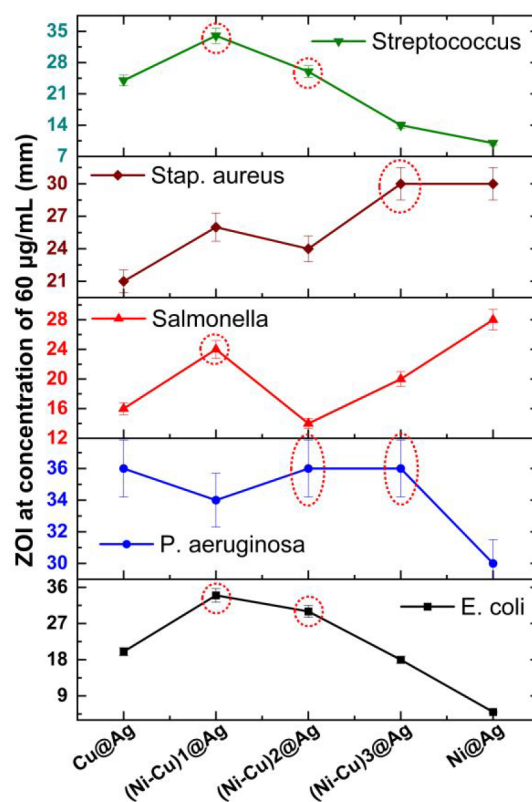
Figure 8. Antibacterial activity of (Ni-Cu)2@Ag NPs against bacteria: (a) *Escherichia coli*; (b) *Pseudomonas aeruginosa*; (c) *Salmonella*; (d) *Staphylococcus aureus*; (e) *Streptococcus*. Numbers refer to the concentrationd of trimetallic NPs: 20, 40, and 60 μg/disk of NPs.
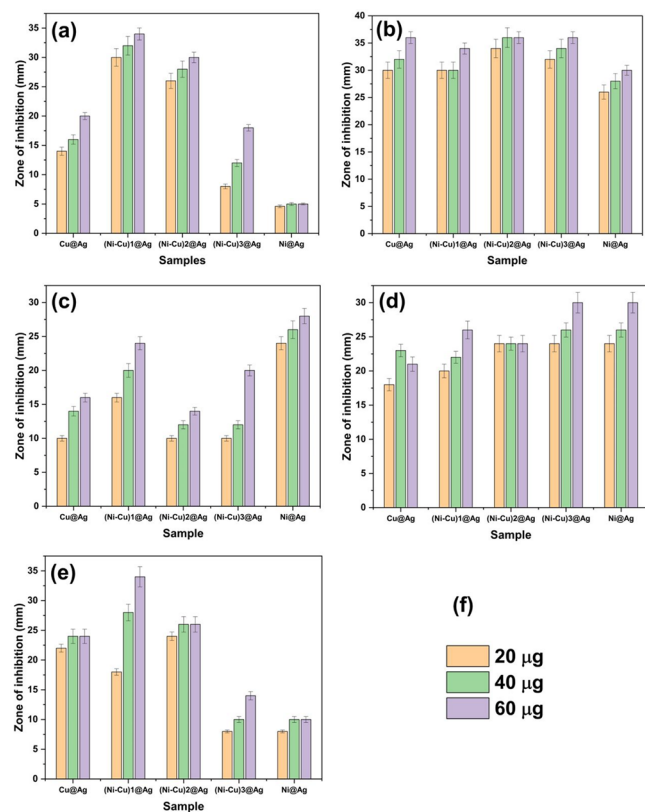
Figure 9. Growth inhibition activity of bi- and trimetallic NPs against various Gram-negative and Gram-positive bacterial pathogens: (a) *Escherichia coli*; (b) *Pseudomonas aeruginosa*; (c) *Salmonella*; (d) *Staphylococcus aureus*; (e) *Streptococcus*; (f) guide to the bar graphs, where the colors correspond to NP concentrations.


Figure 10. Inhibition activity of prepared samples against various Gram-negative and Gram-positive bacterial pathogens at a concentration of 60 μg/mL.

during the oxygen metabolism, which plays a principal role in a number of cellular signaling pathways.[49,50] By adding electrons through the mitochondrial electron transport chain, oxygen is used to synthesize water durin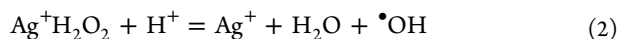g oxidative phosphorylation.[51] Molecular oxygen (O_2) cached some of these electrons to form O_2^-) and thus converted to H_2O_2 and $^\bullet OH$. The ions of metals ($M = Ag^+$, Cu^{2+}, and Ni^{2+}) released by NPs have been shown to

mix into the chemocatalysis and cycling of redox by the Fenton reaction[52]

$$H_2O_2 + M^{x+} \rightarrow M^{(x+1)+} + OH^- + {}^{\bullet}OH \quad (1)$$
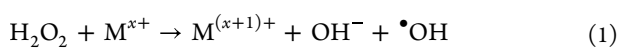
or Fenton-like reaction

$$Ag^+H_2O_2 + H^+ = Ag^+ + H_2O + {}^{\bullet}OH \quad (2)$$

Dissociation of metal ions results in various intracellular processes such as disruption of the bacterial membrane structure, deactivation of enzymes, and disruption of electron shuttling. This is a consequence of the intracellular accumulation of ROS as shown in Scheme 1.

Scheme 1. Production of ROS Induced by Core−Shell NPs in the Surrounding Bacteria Medium
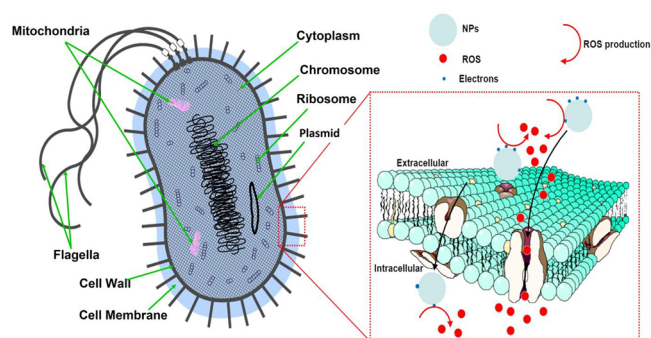
Oxidative stress was induced as a result of the toxicity mechanism that was produced by NPs. Uncoated Ag NPs contributed to the generation of high amounts of hydroxyl and superoxide radicals, while singlet oxygen was generated by Ni NPs.[10] Cu NPs are used widely to generate hydrogen peroxide.[53] This caused several processes such as variation in the membrane potential, intracellular oxidation, disruption of the membrane permeability, cell cycle stopping, DNA damage, protein inactivation, release of cellular contents, and disruption of the electron transfer pathway.[54−60] The overall antibacterial activity of the prepared samples showed that trimetallic NPs improved the inhibition of bacterial growth. In addition, the low concentrations used in this study in comparison to others (Table. 1) is another advantage to avoid the toxicity of higher concentrations of metal NPs. Moreover, the toxicity of trimetallic core−shell NPs against various Gram-negative and Gram-positive bacterial pathogens showed a higher effect of 80−85% compared to standard antibiotics (control), as shown in Figure 11. Thus, this enhancement may make these NPs candidates for promising antibiotic materials.

■ CONCLUSION

In conclusion, this work experimentally evidenced the synthesis of trimetallic (Ni-Cu)@Ag core@shell NPs without stabilizing materials, which has been confirmed by XRD, absorbance, and HRTEM characterizations. The antibacterial activity of the prepared NPs was evaluated against three Gram-negative (*Pseudomonas aeruginosa*, *Escherichia coli*, and *Salmonella*) and two Gram-positive (*Streptococcus* and *Staphylococcus aureus*). The antibacterial activity showed enhancement in the inhibition

Table 1. Comparison of Antibacterial Activity of (Ni-Cu)@Ag Core@Shell NPs with Other Metal and Metal Oxide NPs

nanoparticles (NPs)	assessment method	target bacteria					ref
		E. coli	*P. aeruginosa*	*Salmonella*	*S. aureus*	*Streptococcus*	
		Metal NPs					
Ag NPs	ZOI (mm), 150 μg/mL	15	20		16		61
Ag NPs	ZOI (mm), 215.74 μg/mL	26	19		30		62
Ag NPs	ZOI (mm), concn in mg/mL	15	8		13	14	63
Ag NPs +SiO$_2$ + lignin	ZOI (mm), 150 μg/mL	12	12		12		64
Ag-Ni NPs	ZOI (mm), concn in mg/mL	17	9		15	16	63
Cu@Ag@PANI^a	ZOI (mm), in mg	13			11		65
Ag@GO^b	ZOI (mm), at different AgNO$_3$ conc.	15			14		66
Ag@BSA^c	ZOI (mm)	24	25		26		67
Ag NPs + standard antibiotics	ZOI (mm), Conc. in (mg/mL)	15		13	20		68
Ag@ZrO$_2$	ZOI (mm), 600 μg/mL	15			12		69
Ag-Au/CeO$_2$	ZOI (mm), 100 μg/mL	29			32		70
Ag@TiO$_2$	MIC	200 μg/mL			100 μg/mL		71
Ag@SiO$_2$	MIC	100 μg/mL			100 μg/mL		71
Fe$_3$O$_4$@Ag	MIC	76 μg/mL			356 μg/mL		72
Ni@Ag	antibacterial rate %	60−88%					18
Cu@Ag	ZOI (mm), at different Ag/Cu %	>6			13		20
		Metal Oxides					
CdO	ZOI (mm), 2 mg/mL	13	14		14		45
CdO−NiO−Fe$_2$O$_3$	ZOI (mm), 450 μg/mL	18	25		25		46,47
Ag$_2$O-CeO$_2$−ZnO	ZOI (mm), 500 μg/mL	12	11		11		73
FRGO-Ag-AgO-Ag$_2$O^d	ZOI (mm), 250 mg/mL	16			15		74
ZrO$_2$-Ag$_2$O	ZOI (mm), ZrO$_2$/Ag$_2$O: 1/2 (in M)	15	16		16	14	75
(Ni-Cu)1@Ag	ZOI (mm), 60 μg/mL	34	34	24	26	34	present work
(Ni-Cu)2@Ag	ZOI (mm), 60 μg/mL	30	36	14	24	26	present work
(Ni-Cu)3@Ag	ZOI (mm), 60 μg/mL	18	36	20	30	14	present work

^{a}PANI: Polyaniline. ^{b}GO: Graphene oxide. ^{c}BSA: Bovine Serum Albumin and. ^{d}FRGO: reduced graphene oxide.
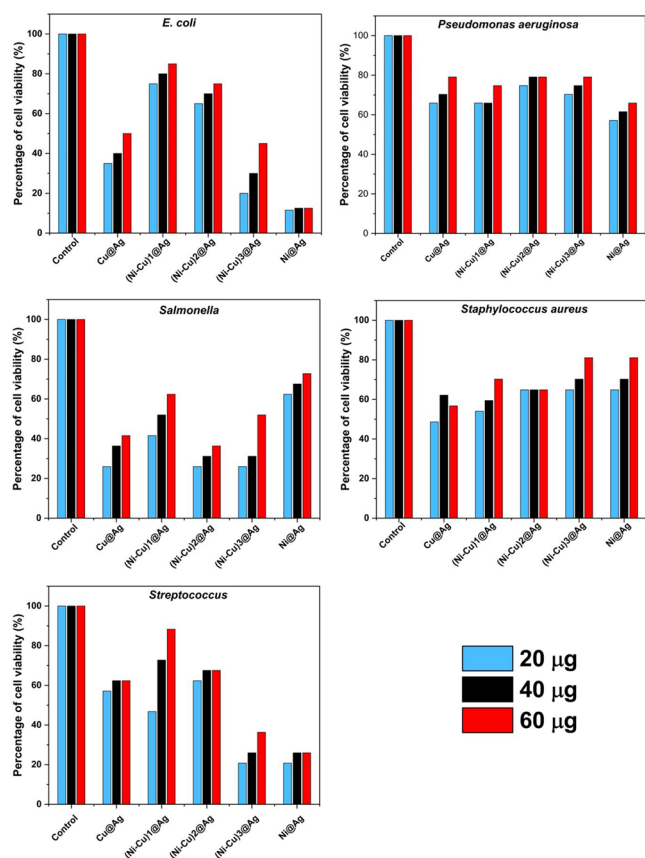
Figure 11. Percentage of cell viability and toxic effect of synthesized bi- and trimetallic NPs against various Gram-negative and Gram-positive bacterial pathogens.

of the bacterial growth due to the synergy of metals in the generation of ROS, which may make these NPs candidates for antibiotic material applications.

ASSOCIATED CONTENT

Data Availability Statement

The data that support the findings of this study are available on request from the corresponding author.

Supporting Information

The Supporting Information is available free of charge at https://pubs.acs.org/doi/10.1021/acsomega.2c03943.

XRD, UV−vis spectra, TXRF, EDS spectra, and additional antibacterial activity measurements (PDF)

AUTHOR INFORMATION

Corresponding Author

Abdullah A. A. Ahmed − *Department of Physics, Faculty of Applied Science, Thamar University, Dhamar 87246, Yemen;* orcid.org/0000-0003-2188-4004; Email: abdullah2803@tu.edu.ye, abdullah2803@gmail.com

Authors

Thana S. Aldeen − *Department of Physics, Faculty of Science, Sana'a University, Sanaa 12544, Yemen*

Samar A. Al-Aqil − *Department of Physics, Faculty of Education & Sciences, Al-Baydha University, Al-Baydha, Yemen*

ZabnAllah M. Alaizeri − *Department of Physics, Faculty of Education & Sciences, Al-Baydha University, Al-Baydha, Yemen*

Saad Megahed − *Department of Physics, Faculty of Science, Al-Azhar University, Cairo, Egypt*

Complete contact information is available at:
https://pubs.acs.org/10.1021/acsomega.2c03943

Notes

The authors declare no competing financial interest.

ACKNOWLEDGMENTS

DEDICATION

The authors dedicate this paper to a member of the author team, Ms. Samar Abdullah Al-Aqil, who passed away while this paper was sent for publication.

REFERENCES

(1) Frieri, M.; Kumar, K.; Boutin, A. Antibiotic resistance. *J. Infect. Public Health* **2017**, *10* (4), 369−378.

(2) Schito, A. M.; Alfei, S. Antibacterial Activity of Non-Cytotoxic, Amino Acid-Modified Polycationic Dendrimers against Pseudomonas aeruginosa and Other Non-Fermenting Gram-Negative Bacteria. *Polymers* **2020**, *12* (8), 1818.

(3) Nel, A.; Xia, T.; Madler, L.; Li, N. Toxic potential of materials at the nanolevel. *science* **2006**, *311* (5761), 622−627.

(4) Xia, T.; Kovochich, M.; Liong, M.; Madler, L.; Gilbert, B.; Shi, H.; Yeh, J. I.; Zink, J. I.; Nel, A. E. Comparison of the mechanism of toxicity of zinc oxide and cerium oxide nanoparticles based on dissolution and oxidative stress properties. *ACS Nano* **2008**, *2* (10), 2121−2134.

(5) Zhao, S.; Li, J.; Cao, D.; Gao, Y.; Huang, W.; Zhang, G.; Sun, R.; Wong, C.-P. Percolation threshold-inspired design of hierarchical multiscale hybrid architectures based on carbon nanotubes and silver nanoparticles for stretchable and printable electronics. *J. Mater. Chem. C* **2016**, *4* (27), 6666−6674.

(6) Lu, Q.; Wang, H.; Liu, Y.; Hou, Y.; Li, H.; Zhang, Y. Graphitic carbon nitride nanodots: as reductant for the synthesis of silver nanoparticles and its biothiols biosensing application. *Biosens. Bioelectron.* **2017**, *89*, 411−416.

(7) Srinivasan, S.; Bhardwaj, V.; Nagasetti, A.; Fernandez-Fernandez, A.; McGoron, A. J. Multifunctional surface-enhanced raman spectroscopy-detectable silver nanoparticles for combined photodynamic therapy and pH-triggered chemotherapy. *J. Biomed. Nanotech* **2016**, *12* (12), 2202−2219.

(8) Zhang, X.-F.; Liu, Z.-G.; Shen, W.; Gurunathan, S. Silver nanoparticles: synthesis, characterization, properties, applications, and therapeutic approaches. *Int. J. Mol. Sci.* **2016**, *17* (9), 1534.

(9) Gupta, A.; Maynes, M.; Silver, S. Effects of halides on plasmid-mediated silver resistance in Escherichia coli. *Appl. Environ. Microbiol.* **1998**, *64* (12), 5042−5045.

(10) Zhang, W.; Li, Y.; Niu, J.; Chen, Y. Photogeneration of reactive oxygen species on uncoated silver, gold, nickel, and silicon nanoparticles and their antibacterial effects. *Langmuir* **2013**, *29* (15), 4647−4651.

(11) Keihan, A. H.; Veisi, H.; Veasi, H. Green synthesis and characterization of spherical copper nanoparticles as organometallic antibacterial agent. *Appl. Organomet. Chem.* **2017**, *31* (7), No. e3642.

(12) Edhari, B. A.; Mashreghi, M.; Makhdoumi, A.; Darroudi, M. Antibacterial and antibiofilm efficacy of Ag NPs, Ni NPs and Al2O3 NPs singly and in combination against multidrug-resistant Klebsiella pneumoniae isolates. *J. Trace Elem. Med. Biol.* **2021**, *68*, 126840.

(13) Gurunathan, S.; Han, J. W.; Kwon, D.-N.; Kim, J.-H. Enhanced antibacterial and anti-biofilm activities of silver nanoparticles against

Gram-negative and Gram-positive bacteria. *Nanoscale Res. Lett.* **2014**, *9* (1), 373.

(14) Murugan, K.; Sanoopa, C. P.; Madhiyazhagan, P.; Dinesh, D.; Subramaniam, J.; Panneerselvam, C.; Roni, M.; Suresh, U.; Nicoletti, M.; Alarfaj, A. A.; Munusamy, M. A.; Higuchi, A.; Kumar, S.; Perumalsamy, H.; Ahn, Y.-J.; Benelli, G. Rapid biosynthesis of silver nanoparticles using Crotalaria verrucosa leaves against the dengue vector Aedes aegypti: what happens around? An analysis of dragonfly predatory behaviour after exposure at ultra-low doses. *Nat. Prod. Res.* **2016**, *30* (7), 826−833.

(15) Lankoff, A.; Sandberg, W. J.; Wegierek-Ciuk, A.; Lisowska, H.; Refsnes, M.; Sartowska, B.; Schwarze, P. E.; Meczynska-Wielgosz, S.; Wojewodzka, M.; Kruszewski, M. The effect of agglomeration state of silver and titanium dioxide nanoparticles on cellular response of HepG2, A549 and THP-1 cells. *Toxicol. Lett.* **2012**, *208* (3), 197−213.

(16) Jiravova, J.; Tomankova, K. B.; Harvanova, M.; Malina, L.; Malohlava, J.; Luhova, L.; Panacek, A.; Manisova, B.; Kolarova, H. The effect of silver nanoparticles and silver ions on mammalian and plant cells in vitro. *Food Chem. Toxicol.* **2016**, *96*, 50−61.

(17) Esquivel-Castro, T. A.; Ibarra-Alonso, M.; Oliva, J.; Martínez-Luévanos, A. Porous aerogel and core/shell nanoparticles for controlled drug delivery: a review. *Mater. Sci. Eng., C* **2019**, *96*, 915−940.

(18) Senapati, S.; Srivastava, S. K.; Singh, S. B.; Mishra, H. N. Magnetic Ni/Ag core-shell nanostructure from prickly Ni nanowire precursor and its catalytic and antibacterial activity. *J. Mater. Chem.* **2012**, *22* (14), 6899−6906.

(19) Ding, X.; Yuan, P.; Gao, N.; Zhu, H.; Yang, Y. Y.; Xu, Q.-H. Au-Ag core-shell nanoparticles for simultaneous bacterial imaging and synergistic antibacterial activity. *Nanotechnol. Biol. Med.* **2017**, *13* (1), 297−305.

(20) Chen, K.-t.; Ray, D.; Peng, Y.-h.; Hsu, Y.-C. Preparation of Cu-Ag core-shell particles with their anti-oxidation and antibacterial properties. *Curr. Appl. Phys.* **2013**, *13* (7), 1496−1501.

(21) Cruces, E.; Arancibia-Miranda, N.; Manquián-Cerda, K.; Perreault, F.; Bolan, N.; Azócar, M. I.; Cubillos, V.; Montory, J.; Rubio, M. A.; Sarkar, B. Copper/Silver Bimetallic Nanoparticles Supported on Aluminosilicate Geomaterials as Antibacterial Agents. *ACS Appl. Nano Mater.* **2022**, *5* (1), 1472−1483.

(22) Tsuji, M.; Yamaguchi, D.; Matsunaga, M.; Ikedo, K. Epitaxial growth of Au@ Ni core- shell nanocrystals prepared using a two-step reduction method. *Cryst. Growth Des* **2011**, *11* (5), 1995−2005.

(23) Tsuji, M.; Nakamura, N.; Ogino, M.; Ikedo, K.; Matsunaga, M. Crystal structures and growth mechanisms of octahedral and decahedral Au@ Ag core-shell nanocrystals prepared by a two-step reduction method. *CrystEngComm* **2012**, *14* (22), 7639−7647.

(24) Kan, C.; Zhu, J.; Wang, C. Ag nanoparticle-filled polymer shell formed around Au nanoparticle core via ultrasound-assisted spherulite growth. *J. Cryst. Growth* **2009**, *311* (6), 1565−1570.

(25) Contreras-Cáceres, R.; Pastoriza-Santos, I.; Alvarez-Puebla, R. A.; Pérez-Juste, J.; Fernández-Barbero, A.; Liz-Marzán, L. M. Growing Au/Ag nanoparticles within microgel colloids for improved surface-enhanced Raman scattering detection. *Chem. - Eur. J.* **2010**, *16* (31), 9462−9467.

(26) Huang, P.; Ma, W.; Yu, P.; Mao, L. Dopamine-Directed In-Situ and One-Step Synthesis of Au@ Ag Core-Shell Nanoparticles Immobilized to a Metal-Organic Framework for Synergistic Catalysis. *Chem. - Asian J.* **2016**, *11* (19), 2705−2709.

(27) Huang, X.; Wu, H.; Pu, S.; Zhang, W.; Liao, X.; Shi, B. One-step room-temperature synthesis of Au@ Pd core-shell nanoparticles with tunable structure using plant tannin as reductant and stabilizer. *Green Chem.* **2011**, *13* (4), 950−957.

(28) Liu, R.; Priestley, R. D. Rational design and fabrication of core-shell nanoparticles through a one-step/pot strategy. *J. Mater. Chem. A* **2016**, *4* (18), 6680−6692.

(29) Zuas, O.; Hamim, N.; Sampora, Y. Bio-synthesis of silver nanoparticles using water extract of *Myrmecodia pendan* (Sarang Semut plant). *Mater. Lett.* **2014**, *123*, 156−159.

(30) Zhu, L.; Cao, M.; Li, L.; Sun, H.; Tang, Y.; Zhang, N.; Zheng, J.; Zhou, H.; Li, Y.; Yang, L.; Zhong, C.-J.; Chen, B. H. Synthesis of Different Ruthenium Nickel Bimetallic Nanostructures and an Investigation of the Structure-Activity Relationship for Benzene Hydrogenation to Cyclohexane. *Chem. Catal. Chem.* **2014**, *6* (7), 2039−2046.

(31) Tao, X.; Sun, L.; Zhao, Y. Sonochemical synthesis and characterization of disk-like copper microcrystals. *Mater. Chem. Phys.* **2011**, *125* (1), 219−223.

(32) Iglesias-Silva, E.; Rivas, J.; León Isidro, L. M.; López-Quintela, M. A. Synthesis of silver-coated magnetite nanoparticles. *J. Non Cryst. Solids* **2007**, *353* (8), 829−831.

(33) Jing, J. J.; Xie, J.; Chen, G. Y.; Li, W. H.; Zhang, M. M. Preparation of nickel-silver core-shell nanoparticles by liquid-phase reduction for use in conductive paste. *J. Exp. Nanosci.* **2015**, *10* (17), 1347−1356.

(34) Tan, S.; Zu, X.; Yi, G.; Liu, X. Synthesis of highly environmental stable copper-silver core-shell nanoparticles for direct writing flexible electronics. *J. Mater. Sci. Mater.* **2017**, *28* (21), 15899−15906.

(35) Shannon, R. D. Revised effective ionic radii and systematic studies of interatomic distances in halides and chalcogenides. *Acta Crystallogr. A* **1976**, *32* (5), 751−767.

(36) Shah, M. Z.; Guan, Z.-H.; Din, A. U.; Ali, A.; Rehman, A. U.; Jan, K.; Faisal, S.; Saud, S.; Adnan, M.; Wahid, F.; Alamri, S.; Siddiqui, M. H.; Ali, S.; Nasim, W.; Hammad, H. M.; Fahad, S. Synthesis of silver nanoparticles using Plantago lanceolata extract and assessing their antibacterial and antioxidant activities. *Sci. Rep.* **2021**, *11* (1), 20754.

(37) Rivera, V.; Ferri, F.; Marega Jr, E., Localized surface plasmon resonances: noble metal nanoparticle interaction with rare-earth ions. In *Plasmonics-Principles and Applications*, Kim, K. Y., Ed.; IntechOpen: 2012; pp 283−312.

(38) Trang, T. N. Q.; Vinh, L. Q.; Doanh, T. T.; Thu, V. T. H. Structure-adjustable colloidal silver nanoparticles on polymers grafted cellulose paper-based highly sensitive and selective SERS sensing platform with analyte enrichment function. *J. Alloys Compd.* **2021**, *867*, 159158.

(39) Chandra, S.; Kumar, A.; Tomar, P. K. Synthesis of Ni nanoparticles and their characterizations. *J. Saudi Chem. Soc.* **2014**, *18* (5), 437−442.

(40) Singh, M.; Sinha, I.; Premkumar, M.; Singh, A. K.; Mandal, R. K. Structural and surface plasmon behavior of Cu nanoparticles using different stabilizers. *Colloids Surf. A Physicochem. Eng. Asp.* **2010**, *359* (1), 88−94.

(41) Jackson, J. B.; Halas, N. J. Silver Nanoshells: Variations in Morphologies and Optical Properties. *J. Phys. Chem. B* **2001**, *105* (14), 2743−2746.

(42) Pajor-Świerzy, A.; Gaweł, D.; Drzymała, E.; Socha, R.; Parlińska-Wojtan, M.; Szczepanowicz, K.; Warszyński, P. The optimization of methods of synthesis of nickel-silver core-shell nanoparticles for conductive materials. *Nanotechnology* **2019**, *30* (1), 015601.

(43) Pinto, V. V.; Ferreira, M. J.; Silva, R.; Santos, H. A.; Silva, F.; Pereira, C. M. Long time effect on the stability of silver nanoparticles in aqueous medium: Effect of the synthesis and storage conditions. *Colloids Surf. A Physicochem. Eng. Asp.* **2010**, *364* (1), 19−25.

(44) Yin, Y.; Li, Z.-Y.; Zhong, Z.; Gates, B.; Xia, Y.; Venkateswaran, S. Synthesis and characterization of stable aqueous dispersions of silver nanoparticles through the Tollens process. *J. Mater. Chem.* **2002**, *12* (3), 522−527.

(45) Ahmed, A. A. A.; Issa, S. A.; Al-Marbie, S. A.; Al-Geraei, M. A.; Al-Mtouakell, H. A.; Al-Mangathi, S. A.; Abduljaleel, J. M.; Qaid, A. A. Structural, optical and antibacterial characteristics of CdO nanostructure prepared via simple method. *Al-Bayadha University J.* **2020**, *2* (2), 9.

(46) Ahmed, A. A. A.; Al-Mushki, A. A. A.; Al-Asbahi, B. A.; Abdulwahab, A. M.; Abduljalil, J. M. A.; Saad, F. A. A.; Qaid, S. M. H.; Ghaithan, H. M.; Farooq, W. A.; Omar, A.-E. H. Effect of ethylene glycol concentration on the structural and optical properties of multimetal oxide CdO-NiO-Fe$_2$O$_3$ nanocomposites for antibacterial activity. *J. Phys. Chem. Solids* **2021**, *155*, 110113.

(47) Al-Mushki, A. A. A.; Ahmed, A. A. A.; Abdulwahab, A. M.; Al-Asbahi, B. A.; Abduljalil, J. M. A.; Saad, F. A. A.; Al-Hada, N. M.; Qaid,

S. M. H.; Ghaithan, H. M. Structural, optical, and antibacterial characteristics of mixed metal oxide CdO-NiO-Fe$_2$O$_3$ nanocomposites prepared using a self-combustion method at different polyvinyl alcohol concentrations. *Appl. Phys. A: Mater. Sci. Process.* **2022**, *128* (4), 279.

(48) Cocheme, H. M.; Murphy, M. P. Mitochondria as a source of reactive oxygen species. *J. Biochem.* **2009**, 1.

(49) Liu, Y.; Imlay, J. A. Cell death from antibiotics without the involvement of reactive oxygen species. *Science* **2013**, *339* (6124), 1210−1213.

(50) Shadel, G. S.; Horvath, T. L. Mitochondrial ROS signaling in organismal homeostasis. *Cell* **2015**, *163* (3), 560−569.

(51) Boonstra, J.; Post, J. A. Molecular events associated with reactive oxygen species and cell cycle progression in mammalian cells. *Gene* **2004**, *337*, 1−13.

(52) Li, Y.; Qin, T.; Ingle, T.; Yan, J.; He, W.; Yin, J.-J.; Chen, T. Differential genotoxicity mechanisms of silver nanoparticles and silver ions. *Arch. Toxicol.* **2017**, *91* (1), 509−519.

(53) Shi, M.; Kwon, H. S.; Peng, Z.; Elder, A.; Yang, H. Effects of Surface Chemistry on the Generation of Reactive Oxygen Species by Copper Nanoparticles. *ACS Nano* **2012**, *6* (3), 2157−2164.

(54) Lee, A.-R.; Lee, S.-J.; Lee, M.; Nam, M.; Lee, S.; Choi, J.; Lee, H.-J.; Kim, D.-U.; Hoe, K.-L. Editor's highlight: a genome-wide screening of target genes against silver nanoparticles in fission yeast. *Toxicol. Sci.* **2018**, *161* (1), 171−185.

(55) Carlson, C.; Hussain, S. M.; Schrand, A. M. K.; Braydich-Stolle, L.; Hess, K. L.; Jones, R. L.; Schlager, J. J. Unique cellular interaction of silver nanoparticles: size-dependent generation of reactive oxygen species. *J. Phys. Chem. B* **2008**, *112* (43), 13608−13619.

(56) Wang, G.; Jin, W.; Qasim, A. M.; Gao, A.; Peng, X.; Li, W.; Feng, H.; Chu, P. K. Antibacterial effects of titanium embedded with silver nanoparticles based on electron-transfer-induced reactive oxygen species. *Biomaterials* **2017**, *124*, 25−34.

(57) Tomankova, K.; Horakova, J.; Harvanova, M.; Malina, L.; Soukupova, J.; Hradilova, S.; Kejlova, K.; Malohlava, J.; Licman, L.; Dvorakova, M. Cytotoxicity, cell uptake and microscopic analysis of titanium dioxide and silver nanoparticles in vitro. *Food Chem. Toxicol.* **2015**, *82*, 106−115.

(58) Kaweeteerawat, C.; Na Ubol, P.; Sangmuang, S.; Aueviriyavit, S.; Maniratanachote, R. Mechanisms of antibiotic resistance in bacteria mediated by silver nanoparticles. *J. Toxicol. Environ. Health Part A* **2017**, *80* (23−24), 1276−1289.

(59) Farah, M. A.; Ali, M. A.; Chen, S.-M.; Li, Y.; Al-Hemaid, F. M.; Abou-Tarboush, F. M.; Al-Anazi, K. M.; Lee, J. Silver nanoparticles synthesized from Adenium obesum leaf extract induced DNA damage, apoptosis and autophagy via generation of reactive oxygen species. *Colloids Surf., B* **2016**, *141*, 158−169.

(60) Ahmed, B.; Hashmi, A.; Khan, M. S.; Musarrat, J. ROS mediated destruction of cell membrane, growth and biofilms of human bacterial pathogens by stable metallic AgNPs functionalized from bell pepper extract and quercetin. *Adv. Powder Technol.* **2018**, *29* (7), 1601−1616.

(61) Adelere, I. A.; Lateef, A.; Aboyeji, D. O.; Abdulsalam, R.; Adabara, N. U.; Bala, J. D. Biosynthesis of silver nanoparticles using aqueous extract of *Buchholzia coriacea* (wonderful kola) seeds and their antimicrobial activities. *Annals. Food Science and Technology* **2017**, *18* (4), 671−679.

(62) Guzman, M.; Dille, J.; Godet, S. Synthesis and antibacterial activity of silver nanoparticles against gram-positive and gram-negative bacteria. *Nanomed.: Nanotechnol. Biol. Med.* **2012**, *8* (1), 37−45.

(63) Akinsiku, A. A.; Dare, E. O.; Ajanaku, K. O.; Ajani, O. O.; Olugbuyiro, J. A. O.; Siyanbola, T. O.; Ejilude, O.; Emetere, M. E. Modeling and Synthesis of Ag and Ag/Ni Allied Bimetallic Nanoparticles by Green Method: Optical and Biological Properties. *Int. J. Biomater.* **2018**, *2018*, 9658080.

(64) Klapiszewski, Ł.; Rzemieniecki, T.; Krawczyk, M.; Malina, D.; Norman, M.; Zdarta, J.; Majchrzak, I.; Dobrowolska, A.; Czaczyk, K.; Jesionowski, T. Kraft lignin/silica-AgNPs as a functional material with antibacterial activity. *Colloids Surf., B* **2015**, *134*, 220−228.

(65) Mohsen, R.; Mohamed, S.; Abu-ayana, Y.; Ghoneim, A. Synthesis of Conductive Cu-core/Ag-subshell/polyaniline-shell Nanocomposites and their Antimicrobial Activity. *Egypt. J. Chem.* **2018**, *61* (5), 939−952.

(66) Huang, L.; Yang, H.; Zhang, Y.; Xiao, W. Study on Synthesis and Antibacterial Properties of Ag NPs/GO Nanocomposites. *J. Nanomater.* **2016**, *2016*, 5685967.

(67) Mathew, T. V.; Kuriakose, S. Studies on the antimicrobial properties of colloidal silver nanoparticles stabilized by bovine serum albumin. *Colloids Surf. B Biointerfaces* **2013**, *101*, 14−18.

(68) Singh, P.; Singh, H.; Kim, Y. J.; Mathiyalagan, R.; Wang, C.; Yang, D. C. Extracellular synthesis of silver and gold nanoparticles by Sporosarcina koreensis DC4 and their biological applications. *Enzyme Microb. Technol.* **2016**, *86*, 75−83.

(69) Dhanalekshmi, K.; Meena, K. DNA intercalation studies and antimicrobial activity of Ag@ ZrO$_2$ core-shell nanoparticles in vitro. *Mater. Sci. Eng., C* **2016**, *59*, 1063−1068.

(70) Nithya, P.; Sundrarajan, M. Ionic liquid functionalized biogenic synthesis of AgAu bimetal doped CeO$_2$ nanoparticles from Justicia adhatoda for pharmaceutical applications: Antibacterial and anti-cancer activities. *J. Photochem. Photobiol. B: Biol.* **2020**, *202*, 111706.

(71) Dhanalekshmi, K.; Meena, K. Comparison of antibacterial activities of Ag@ TiO2 and Ag@ SiO2 core-shell nanoparticles. *Spectrochim. Acta - A: Mol. Biomol. Spectrosc.* **2014**, *128*, 887−890.

(72) Chudasama, B.; Vala, A. K.; Andhariya, N.; Upadhyay, R. V.; Mehta, R. V. Enhanced antibacterial activity of bifunctional Fe$_3$O$_4$-Ag core-shell nanostructures. *Nano Res.* **2009**, *2* (12), 955−965.

(73) Subhan, M. A.; Uddin, N.; Sarker, P.; Nakata, H.; Makioka, R. Synthesis, characterization, low temperature solid state PL and photocatalytic activities of Ag$_2$O·CeO$_2$·ZnO nanocomposite. *Spectrochim. Acta - A: Mol. Biomol. Spectrosc.* **2015**, *151*, 56−63.

(74) Lekshmi, G. S.; Tamilselvi, R.; Geethalakshmi, R.; Kirupha, S. D.; Bazaka, O.; Levchenko, I.; Bazaka, K.; Mandhakini, M. Multifunctional oil-produced reduced graphene oxide - Silver oxide composites with photocatalytic, antioxidant, and antibacterial activities. *J. Colloid Interface Sci.* **2022**, *608*, 294−305.

(75) Ayanwale, A. P.; Ruíz-Baltazar, A. d. J.; Espinoza-Cristóbal, L.; Reyes-López, S. Y. Bactericidal Activity Study of ZrO$_2$-Ag$_2$O Nanoparticles. *Dose-Response* **2020**, *18* (3), 1−13.